Science Bulletin xxx (xxxx) xxx

Contents lists available at ScienceDirect

Science Bulletin

journal homepage: www.elsevier.com/locate/scib

Short Communication

Structural insights and engineering of deep-sea halophilic PET hydrolytic enzymes

Guoqiang Zhang [a,b,c,1], Xian Li [d,e,1], Wei Xia [f,1], Chengsong Zhang [a,b], Shanmin Zheng [a,c], Hongchen Yin [a], Jieke Du [a], Ning Wang [a], Xinzhe Chen [a,g], Ge Lv [a], Yushuo Zhao [a], Tianheng Wang [a], Yunjun Pan [a,c], Mingzhu Zhang [e], Jian-Wen Huang [d], Chun-Chi Chen [d], Siqi Huang [e], Cheng Zeng [e], Zhengquan Gao [g], Jianwei Chen [h], Di Wang [h], Guangyi Fan [h], Xingwang Zhang [a], Yaohua Zhong [a,i], Hongliang Wang [b], Xue-Wei Xu [b], Yongfu Sun [b], Xiujuan Li [j], He Huang [j], Jing Wu [f,*], Kun Liu [a,c,i,*], Rey-Ting Guo [d,*], Shengying Li [a,c,*]

[a] State Key Laboratory of Microbial Technology, Shandong University, Qingdao 266237, China
[b] National Deep Sea Center, Qingdao 266237, China
[c] Laboratory for Marine Biology and Biotechnology, Qingdao Marine Science and Technology Center, Qingdao 266237, China
[d] Zhejiang Key Laboratory of Medical Epigenetics, Department of Immunology and Pathogen Biology, School of Basic Medical Sciences, Hangzhou Normal University, Hangzhou 311121, China
[e] Hubei Hongshan Laboratory, School of Life Sciences, Hubei University, Wuhan 430062, China
[f] School of Biotechnology and Key Laboratory of Industrial Biotechnology Ministry of Education, Jiangnan University, Wuxi 214122, China
[g] School of Pharmacy, Binzhou Medical University, Yantai 264003, China
[h] BGI Research, Qingdao 266555, China
[i] Gan Su Institute of Shandong University, Lanzhou 730000, China
[j] State Key Laboratory of Microbial Technology, School of Food Science and Pharmaceutical Engineering, Nanjing Normal University, Nanjing 210097, China

ARTICLE INFO

Article history:
Received 25 March 2026
Received in revised form 30 July 2026
Accepted 28 September 2026
Available online xxxx

© 2026 Science China Press. Published by Elsevier B.V. and Science China Press. All rights are reserved, including those for text and data mining, AI training, and similar technologies.

The widespread use and recalcitrance of polyethylene terephthalate (PET) have led to its extensive environmental accumulation [1,2]. Enzymatic depolymerization has emerged as a sustainable recycling method by converting PET into reusable monomers (Fig. S1 online). Progress has been driven by the discovery of novel enzymes from diverse environments [3]. Enzymes from extreme habitats, including composts and glaciers [4,5], can retain high activity under harsh conditions. Deep-sea ecosystems, characterized by high salinity, low temperature, and elevated pressure, therefore represent an underexplored source of robust biocatalysts. Recently, we reported three high-performance PETases from deep-sea metagenomes that require high NaCl concentrations for optimal activity [6].

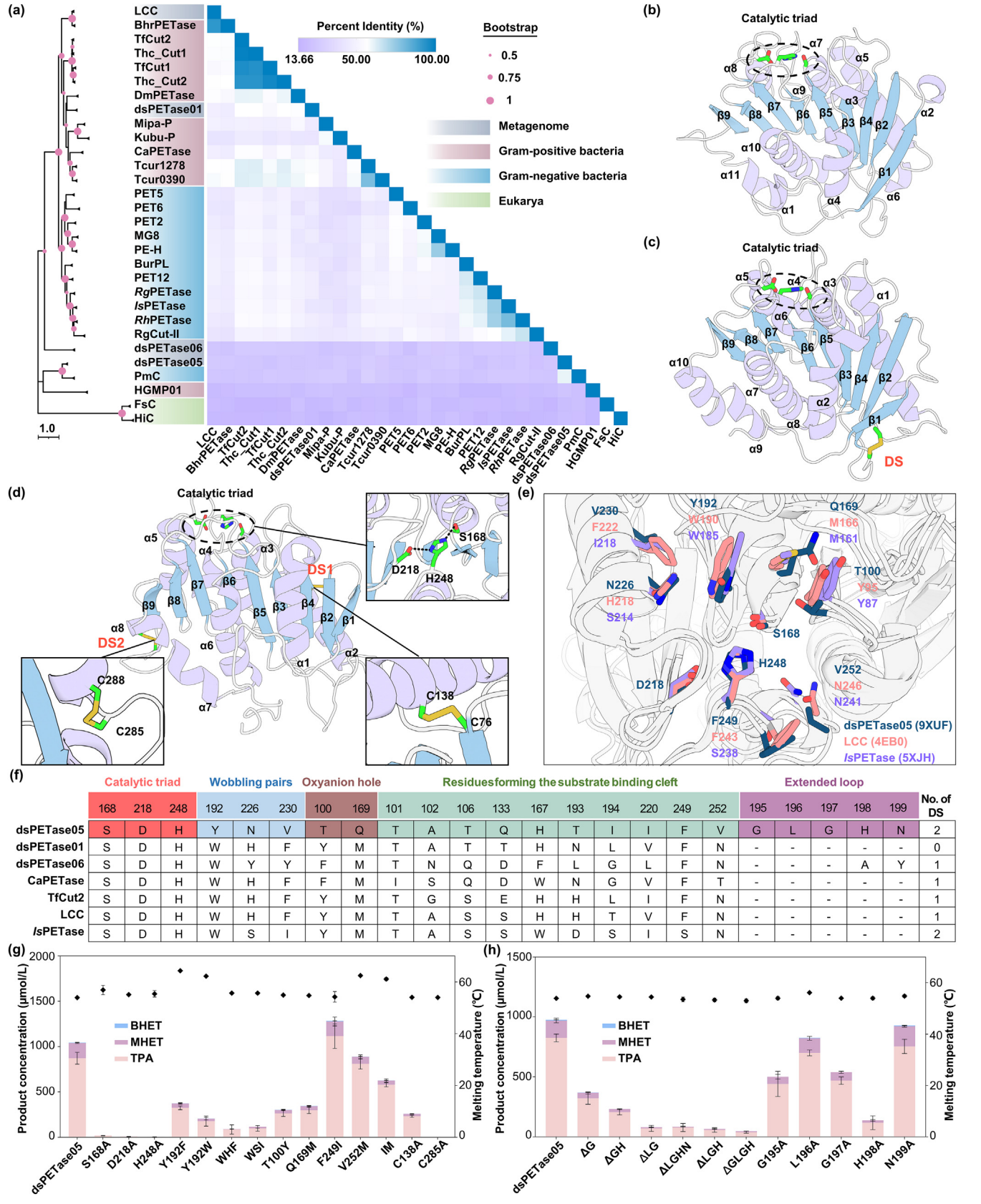
To assess their evolutionary relationships, we compared dsPETase01, dsPETase05, and dsPETase06 with 27 reported PET hydrolases (Fig. 1a). The phylogeny separated known PET hydrolases into bacterial and fungal lineages, with the three deep-sea PETases showing divergent placements. dsPETase01 grouped with Gram-positive bacterial hydrolases, whereas dsPETase05 and dsPETase06 were closer to fungal PET hydrolases and outside the major bacterial clusters. Notably, dsPETase05 was most closely related to PmC [7], whereas dsPETase06 occupied an independent branch, suggesting distinct evolutionary origins among these deep-sea PETases.

To characterize their structural features, we determined their high-resolution crystal structures (Table S1 online). All three enzymes adopt the canonical α/β-hydrolase fold, yet display several distinctive structural features. dsPETase01 was solved at 1.61 Å resolution in space group $P2_1$ (PDB ID #: 9XUE), with two chains observed in an asymmetric unit (Fig. 1b and Fig. S2 online). The structure comprises a central twisted β-sheet composed of nine β-strands flanked on both sides by eleven α-helices. The conserved catalytic triad S159-D205-H237 is consistent with other PET hydrolases [8], yet no disulfide bond is observed. For dsPETase06, the C23A mutant yielded a 1.38 Å structure, though resi-

* Corresponding authors.
E-mail addresses: jingwu@jiangnan.edu.cn (J. Wu), liuk@sdu.edu.cn (K. Liu), guoreyting@hznu.edu.cn (R.-T. Guo), lishengying@sdu.edu.cn (S. Li).
[1] These authors contributed equally to this work.

https://doi.org/10.1016/j.scib.2026.09.079
2095-9273/© 2026 Science China Press. Published by Elsevier B.V. and Science China Press. All rights are reserved, including those for text and data mining, AI training, and similar technologies.

Please cite this article as: G. Zhang, X. Li, W. Xia et al., Structural insights and engineering of deep-sea halophilic PET hydrolytic enzymes, Science Bulletin, https://doi.org/10.1016/j.scib.2026.09.079



	Catalytic triad			Wobbling pairs			Oxyanion hole		Residues forming the substrate binding cleft										Extended loop					No. of DS
	168	218	248	192	226	230	100	169	101	102	106	133	167	193	194	220	249	252	195	196	197	198	199	
dsPETase05	S	D	H	Y	N	V	T	Q	T	A	T	Q	H	T	I	I	F	V	G	L	G	H	N	2
dsPETase01	S	D	H	W	H	F	Y	M	T	A	T	T	H	N	L	V	F	N	-	-	-	-	-	0
dsPETase06	S	D	H	W	Y	Y	F	M	T	N	Q	D	F	L	G	L	F	N	-	-	-	A	Y	1
CaPETase	S	D	H	W	H	F	F	M	I	S	Q	D	W	N	G	V	F	T	-	-	-	-	-	1
TfCut2	S	D	H	W	H	F	Y	M	T	G	S	E	H	H	L	I	F	N	-	-	-	-	-	1
LCC	S	D	H	W	H	F	Y	M	T	A	S	S	H	H	T	V	F	N	-	-	-	-	-	1
*Is*PETase	S	D	H	W	S	I	Y	M	T	A	S	S	W	D	S	I	S	N	-	-	-	-	-	2

Fig. 1. Phylogenetic and structural analysis of three halophilic PET hydrolases and validation of dsPETase05 features. (a) Phylogenetic tree and identity matrix of 30 PETase sequences. Bootstrap values are indicated by pink circles (1000 replicates). (b) Canonical α/β-hydrolase fold of dsPETase01 (PDB ID #: 9XUE). (c) dsPETase06_C23A (PDB ID #: 9XUI) with the only disulfide bond (yellow sticks). (d) dsPETase05 (PDB ID #: 9XUF) with the two disulfide bonds (yellow sticks), catalytic residues highlighted (top right). (e) Spatial distribution of critical residues in dsPETase05, LCC, and *Is*PETase. (f) Comparison of key residues, extended loop, and disulfide-bond numbers. (g) Mutagenesis analysis of critical residues. (h) Amino acid residue deletion and alanine scanning mutagenesis of the extended loop. Assays: amorphous PET film (6 mm in diameter), 50 nmol/L enzyme, 5.3 mol/L NaCl, pH 9.0 Tris-HCl buffer, 24 h; wild-type dsPETase05 served as the control. Enzymatic activity (product yield, bars) and melting temperature (T_m, diamonds) are shown. Structural schematics and data plots were generated using PyMOL and GraphPad Prism, respectively.

dues 23–34 at the *N*-terminus remained unresolved (PDB ID #: 9XUI). The refined model features ten α-helices surrounding a 9-stranded β-sheet core, and harbors a single intramolecular disulfide bond (C47–C67) near the *N*-terminal domain (Fig. 1c).

Structural characterization of dsPETase05, the most catalytically efficient among the three halophilic dsPETases [6], revealed distinctive molecular features. The crystal structure, determined at 2.06 Å resolution (space group $I2_13$), contains a single molecule in the asymmetric unit (PDB ID #: 9XUF). The enzyme adopts a canonical α/β-hydrolase fold comprising nine β-strands flanked by eight α-helices. Two intramolecular disulfide bonds exist: DS1 (C76–C138) stabilizes the *N*-terminal domain, while DS2 (C285–C288) reinforces the *C*-terminal region (Fig. 1d).

We next compared surface hydrophobicity and charge distributions of the three halophilic dsPETases with *Is*PETase and LCC (Fig. S3 online). While all five enzymes possess similar hydrophobic pockets, their global and local surface charge distributions differ markedly. Such disparities are likely to influence substrate recognition and catalytic efficiency. In addition, dsPETase05 shows the greatest structural divergence, as evidenced by the root mean square deviation (RMSD) values when aligned with the other PETases (Fig. S4 online).

To probe enzyme-substrate interactions, we obtained complex structures by co-crystallizing wild-type dsPETase05 with the product terephthalic acid (TPA) (1.5 Å, PDB ID #: 9XUG) and an inactive mutant (S168A) with TPA (1.49 Å, PDB ID #: 9XUH). Comparative analysis revealed minimal structural perturbation (Cα RMSD = 0.097 Å) between the two complexes (Fig. S5 online), although subtle differences in ligand position and the conformational flexibility of T100/T101 were observed. Well-defined electron density and the Fo-Fc maps confirm that the modeled active-site residues and ligand are reliably interpreted from the crystallographic data (Fig. S6 online). The substrate-binding cleft contains a conserved aromatic-hydrophobic pocket formed by Y192, V252, F249, H167, T100, and Q169.

Structural alignment with LCC and *Is*PETase revealed that dsPETase05 retains the conserved catalytic triad (S168–D218–H248), but differs in the oxyanion hole, wobbling pairs (conformationally flexible residues involved in substrate accommodation [8]), substrate-binding regions, and disulfide bond configurations (Fig. 1e). Sequence and structural comparisons further identified a unique extended loop near the active site in dsPETase05 (Fig. S7 online). Site-directed mutagenesis and activity assays then systematically evaluated the catalytic contributions of these features (Fig. 1f).

Alanine substitution of any catalytic triad residue (S168A, D218A, or H248A) nearly abolished activity, confirming their essential role (Fig. 1g). Disrupting either disulfide bond with C138A or C285A mutations significantly reduced PET hydrolytic activity, particularly for C285A (Fig. 1g). Thus, both disulfide bonds are critical for dsPETase05 structural integrity and catalytic function.

The dsPETase05 oxyanion hole differs substantially from those of LCC and *Is*PETase: T100 and Q169 correspond to Y95 and M166 in LCC and Y87 and M161 in *Is*PETase, respectively (Fig. 1e). Moreover, dsPETase05 Y192 replaces the tryptophan conserved at the equivalent position in LCC (W190) and *Is*PETase (W185), which is critical in PET hydrolysis [8,9].

To evaluate the functional impact of these differences, we performed site-directed mutagenesis analysis. The T100Y, Q169M, Y192F, and Y192W mutants retained only 29.1%, 33.2%, 35.9%, and 19.8% of wild-type activity, respectively (Fig. 1g). The WSI (Y192W/N226S/V230I) and WHF (Y192W/N226H/V230F) combinations further reduced activity to 11.2% and 8.7%. These results collectively demonstrate that dsPETase05 possesses a unique oxyanion hole architecture and tyrosine residue configuration.

Inspired by LCC-ICCG [1], we introduced F249I, V252M, and the combined F249I/V252M (IM) mutations in the substrate-binding pocket of dsPETase05. Only F249I improved activity by approximately 1.2-fold over wild-type (Fig. 1g), and this position was selected for further enzyme engineering. To investigate the functional relevance of the extended loop in dsPETase05, we performed both amino acid deletion and alanine scanning mutagenesis. Sequential deletion of residues from this loop resulted in a progressive decline in enzymatic activity under high-salt conditions (Fig. 1h), indicating that this loop is crucial for maintaining enzyme structure and/or catalytic function. Alanine scanning further identified H198 as essential for enzymatic activity.

Sequence and structure analysis of dsPETase05 revealed a total of 18 acidic residues, 10 of which are located in the *C*-terminal region, specifically after the last catalytic triad residue H248 (Fig. 2a). In contrast, *Is*PETase, which we have previously demonstrated to be non-halotolerant [6], contains only 12 acidic residues, five of which are located in the *C*-terminal region following H237 (Fig. 2b). To assess their functional significance, we generated 18 reciprocal *C*-terminal chimeras between dsPETase05 and *Is*PETase (Fig. 2c). Notably, substitution of the *C*-terminal region of dsPETase05 with that of *Is*PETase—which is relatively depleted in acidic residues—resulted in chimeric enzymes exhibiting significantly enhanced catalytic activity under salt-free conditions compared to wild-type dsPETase05 (Fig. 2d). In contrast, transplantation of the acidic residue-rich *C*-terminal regions from dsPETase05 into *Is*PETase conferred partial salt tolerance to the resulting chimeric enzymes (Isd257 and Isd277). Under 5.3 mol/L NaCl, these variants exhibited higher activity than native *Is*PETase; however, the difference was not statistically significant (Fig. 2e). These results suggested that the contribution of *C*-terminal acidic residues to salt adaptation depends not simply on their number but also on their specific positions and structural context. The distinct catalytic behaviors of the chimeric enzymes indicated that only specific crossover boundaries are structurally tolerated, implying that the *C*-terminal region contains both transferable salt-adaptive elements and structurally constrained sites.

To further delineate the specific acidic residues, six progressively substituted variants (dsIr1–dsIr6) were generated by replacing *C*-terminal acidic residues of dsPETase05 with the corresponding *Is*PETase residues (Table S2 online for details). At 5.3 mol/L NaCl, dsIr6 exhibited sharply decreased activity compared to dsPETase05 and other mutants (Fig. S8a online), indicating that D273 plays an important role in maintaining halotolerance. In contrast, under salt-free conditions, the dsIr5 mutant displayed increased activity relative to dsPETase05, other mutants, and *Is*PETase (Fig. S8b online). NaCl gradient assays further showed that dsIr6 did not exhibit a shifted salt optimum but instead displayed reduced activity across the tested salt concentrations, supporting the essential role of D273 in maintaining halophilic activity (Fig. S8c online).

Consistently, the single D273N mutant showed markedly reduced activity compared with wild-type dsPETase05 (Fig. S9 online). D273 is located at the boundary region between the protein surface and the inner core near the catalytic pocket, and its substitution with Asn may disrupt local hydrogen bonding, salt-bridge interactions, or neighboring loop conformations, thereby destabilizing the active-site microenvironment. To further elucidate the halophilic mechanism under high-salt conditions, we performed molecular dynamics simulations on dsPETase05 (Fig. S10 online). The results revealed that the salt-induced rigidification and compact pocket architecture maintained the integrity of the spatial arrangement of key substrate-recognition residues, thereby facilitating stable substrate binding and providing a favorable structural microenvironment for catalysis.

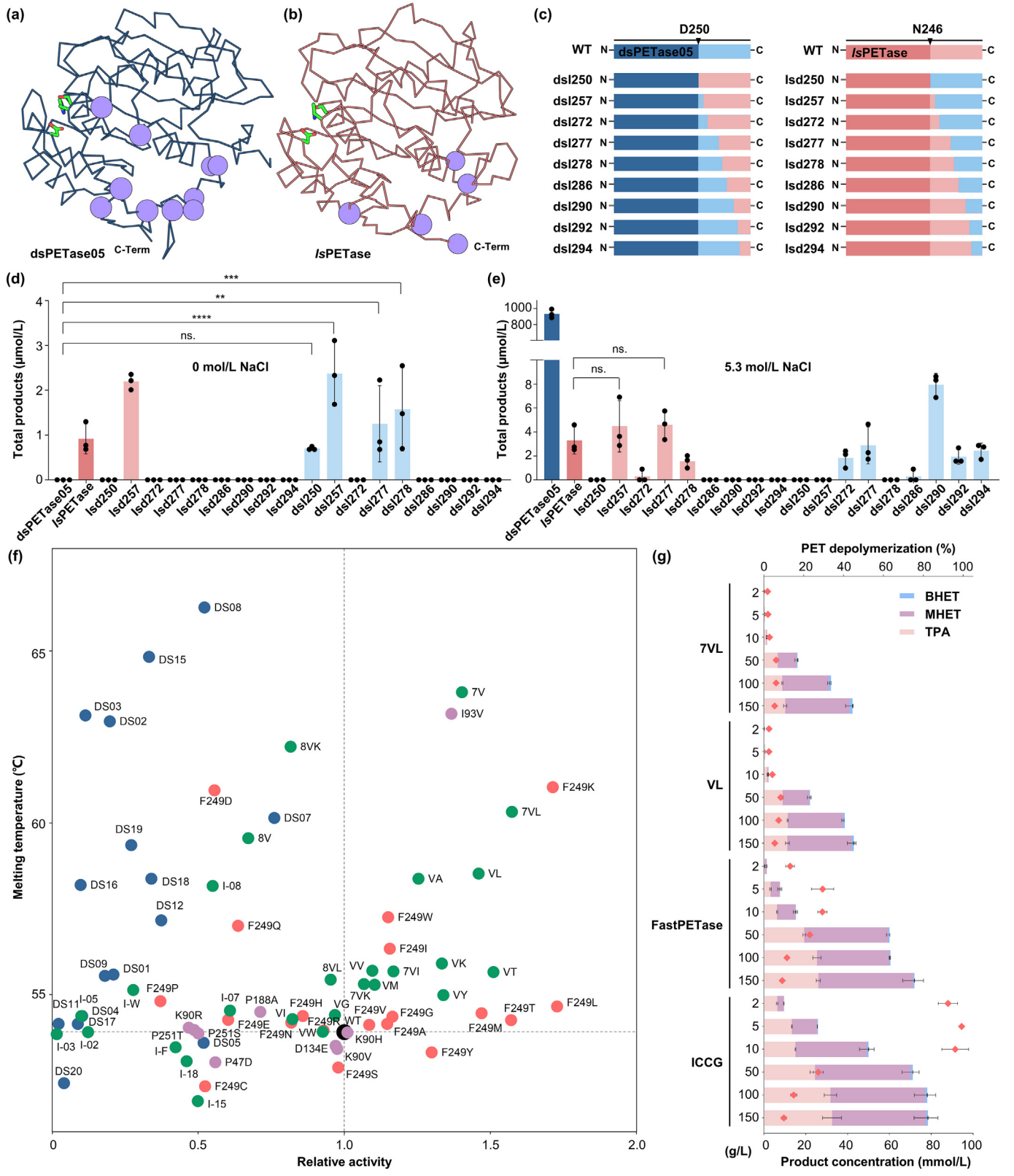


Fig. 2. Enzyme engineering of dsPETase05. *C*-terminal acidic residues (purple spheres) in dsPETase05 (a) and *Is*PETase (b). (c) Schematic exchange of *C*-terminal regions in different lengths of dsPETase05 and *Is*PETase; activities of *C*-terminal domain-swapped mutants under 0 mol/L NaCl (d) and 5.3 mol/L NaCl (e). Statistical analysis was performed using one-way ANOVA followed by Tukey's post hoc test; ns., $P > 0.05$; $^{**}P < 0.01$; $^{***}P < 0.001$; $^{****}P < 0.0001$. (f) Melting temperature (T_m) and relative PET degradation activity of dsPETase05 variants. Colors: wild type (black), Transformer-predicted substitutions (lilac), F249 saturation mutagenesis (salmon), disulfide bond-engineered variants (dark blue), and combinatorial mutants (green). (g) PET powder degradation by 7VL, VL, FastPETase, and ICCG at 0.2%–15% (*w*/*w*) substrate loading, with 1 mg enzyme gPET^{-1}. Conditions: 7VL and VL, 5.3 mol/L NaCl, 55 ℃, 50 mmol/L Tris-HCl (pH 9.0); FastPETase, 50 ℃, 0.1 mol/L phosphate buffer (pH 8.0); ICCG, 72 ℃, 0.1 mol/L phosphate buffer (pH 8.0). Bars show product concentrations and diamonds show PET depolymerization. Structural schematics and data plots were generated using PyMOL and GraphPad Prism, respectively.

We next engineered dsPETase05 using three complementary strategies: (1) transformer-guided prediction of candidate mutation sites [10], followed by high-throughput fluorescence screening [11] (Fig. S11 online); (2) saturation mutagenesis at F249 to identify beneficial substitutions (Fig. S12 online); and (3) homology-guided disulfide bond engineering [12] to identify candidate residue pairs (Fig. S13 and Table S3 online).

The Transformer model predicted 45 candidate residues to improve catalytic activity. An NNK-based saturation mutagenesis library was constructed for each site, yielding ~4500 variants in total. Through high-throughput fluorescence screening, nine beneficial mutants distributed across six sites were identified (Fig. S14 online). Purified enzyme assays showed that only I93V improved both catalytic activity and melting temperature (T_m), while others performed comparably or worse than dsPETase05 (Fig. 2f, lilac markers). I93V was therefore selected for further combinatorial mutagenesis.

In dsPETase05, F249 lies near the catalytic H248. The F249I substitution increased activity, likely by reducing steric hindrance and improving substrate access to the active site [1]. Saturation mutagenesis at F249 yielded nine mutants with both higher activity and increased T_m, among which F249K showed the greatest combined improvement (Fig. 2f). Inspired by the enhanced activity and thermostability of LCC-ICCG engineering [1], we engineered 15 disulfide bonds in dsPETase05. Most variants had increased T_m but reduced catalytic activity (Fig. 2f, dark blue circles).

To balance the trade-off between enhanced thermostability and catalytic activity, we further combined the beneficial single-point mutations (such as I93V and F249L) with selected disulfide bond mutants that exhibited notable increases in T_m, resulting in 26 soluble mutants (Table S4 online). As a result, the 7V mutant (DS07/I93V) achieved a ΔT_m of 9.9 ℃ and exhibited a 1.4-fold increase in PET hydrolytic activity. Notably, the 7VL variant (DS07/I93V/F249L) maintained a ΔT_m of 6.4 ℃ while demonstrating nearly 1.6-fold improvement in PET-specific activity (Fig. 2f).

We further benchmarked VL and 7VL on amorphous PET powder against FastPETase [13] and ICCG [1] (Fig. 2g and Fig. S15 online). VL and 7VL reached maximal PET degradation yields of 8.4% and 6.2%, respectively, at 5% (*w*/*w*) PET loading, whereas FastPETase and ICCG achieved yields of 29.5% and 99.2%, respectively, at 0.5% (*w*/*w*) PET loading. Time-course data showed that FastPETase and ICCG approached their maximum degradation yields within 3 h, whereas the yields of VL and 7VL continued to increase over 24 h before reaching a plateau. Thus, VL and 7VL are active on amorphous PET powder but lag behind FastPETase and ICCG in both rate and final conversion under the tested conditions. Nevertheless, their sustained activity over 24 h suggests this halophilic scaffold is a promising base for further engineering toward higher yields, though the plateau indicates a remaining limitation.

In summary, we present the structures and mechanistic characterization of three deep-sea halophilic PET hydrolases. Through structural analysis, mutagenesis, domain swapping, Transformer-based modeling, semi-rational design, and disulfide bond engineering, we enhanced the thermostability and catalytic efficiency of dsPETase05, providing a framework for engineering PET biocatalysts active across broader ionic-strength conditions. Although the high NaCl requirement of dsPETases may increase industrial processing costs, strategies such as salt recycling, integration with saline process streams, or the use of natural brine could help mitigate this limitation. In addition, their salt-dependent catalysis may offer an intrinsic activity-switch mechanism for applications requiring spatial or temporal control of PET hydrolysis.

Conflict of interest

The authors declare that they have no conflict of interest.

Acknowledgments

This work was financially supported by the National Key Research and Development Project of China (2025YFA0923200), National Natural Science Foundation of China (32370124, 32571710, and 32025001), Key R&D Program of Shandong Province, China (2025CXPT190), Shandong Provincial Natural Science Foundation, China (ZR2023ZD50), SKLMT Frontiers and Challenges Project (SKLMTFCP-2023-02), Qingdao Natural Science Foundation, China (25-3-1-8-zyyd-jch-1), Youth Student Fundamental Research Funds of Shandong University (SDUQM2504), Natural Science Foundation of Shandong Province, China (ZR2026QC0253), Guangdong Basic and Applied Basic Research Foundation, China (2025B1515020038), and Binzhou's "Revealing List & Taking Lead" Key Technology Research Projects, China (2025JBGS001). We thank Chengjia Zhang and Yunhui Lu from the Core Facilities for Life and Environmental Sciences, State Key Laboratory of Microbial Technology of Shandong University, for their technical assistance with bioreactor operation.

Author contributions

Kun Liu, Rey-Ting Guo, Jing Wu, and Shengying Li conceived the research. Guoqiang Zhang, Wei Xia, Chengsong Zhang, Shanmin Zheng, Hongchen Yin, Jieke Du, Ning Wang, Xinzhe Chen, Ge Lv, Yushuo Zhao, and Tianheng Wang performed most of the bioinformatics analyses and mutation experiments. Xian Li, Mingzhu Zhang, Jian-Wen Huang, Chun-Chi Chen, Siqi Huang, and Cheng Zeng determined all the protein structures. Guoqiang Zhang, Xian Li, and Kun Liu analyzed the results. Yunjun Pan, Zhengquan Gao, Jianwei Chen, Di Wang, Guangyi Fan, Xingwang Zhang, Yaohua Zhong, Hongliang Wang, Xue-Wei Xu, Yongfu Sun, Xiujuan Li, and He Huang provided comments and suggestions on the paper. The paper was written and revised jointly by all the authors.

Data availability

The atomic coordinates and structure factors have been deposited in the Protein Data Bank (https://www.rcsb.org/) under accession codes 9XUE, 9XUF, 9XUG, 9XUH, and 9XUI for dsPETase01_apo, dsPETase05_apo, dsPETase05_TPA, dsPETase05_S168A_TPA, and dsPETase06_C23A_apo, respectively.

Appendix A. Supplementary material

Supplementary data to this article can be found online at https://doi.org/10.1016/j.scib.2026.09.079.

References

[1] Tournier V, Topham CM, Gilles A, et al. An engineered PET depolymerase to break down and recycle plastic bottles. Nature 2020;580:216–9.
[2] Wei R, Westh P, Weber G, et al. Standardization guidelines and future trends for PET hydrolase research. Nat Commun 2025;16:4684.
[3] Buchholz PCF, Feuerriegel G, Zhang H, et al. Plastics degradation by hydrolytic enzymes: the plastics-active enzymes database-PAZy. Proteins 2022;90:1443–56.
[4] Qi X, Ji M, Yin C-F, et al. Glacier as a source of novel polyethylene terephthalate hydrolases. Environ Microbiol 2023;25:2822–33.
[5] Sulaiman S, Yamato S, Kanaya E, et al. Isolation of a novel cutinase homolog with polyethylene terephthalate-degrading activity from leaf-branch compost by using a metagenomic approach. Appl Environ Microbiol 2012;78:1556–62.
[6] Chen J, Jia Y, Sun Y, et al. Global marine microbial diversity and its potential in bioprospecting. Nature 2024;633:371–9.

[7] Ronkvist ÅM, Xie W, Lu W, et al. Cutinase-catalyzed hydrolysis of poly (ethylene terephthalate). Macromolecules 2009;42:5128–38.
[8] Han X, Liu W, Huang J-W, et al. Structural insight into catalytic mechanism of PET hydrolase. Nat Commun 2017;8:2106.
[9] Chen C-C, Han X, Li X, et al. General features to enhance enzymatic activity of poly(ethylene terephthalate) hydrolysis. Nat Catal 2021;4:425–30.
[10] Cui Y, Chen Y, Sun J, et al. Computational redesign of a hydrolase for nearly complete PET depolymerization at industrially relevant high-solids loading. Nat Commun 2024;15:1417.
[11] Liu K, Xu Z, Zhao Z, et al. A dual fluorescence assay enables high-throughput screening for poly(ethylene terephthalate) hydrolases. ChemSusChem 2023;16:e202202019.
[12] Suplatov D, Timonina D, Sharapova Y, et al. Yosshi: a web-server for disulfide engineering by bioinformatic analysis of diverse protein families. Nucleic Acids Res 2019;47:W308–14.
[13] Lu H, Diaz DJ, Czarnecki NJ, et al. Machine learning-aided engineering of hydrolases for PET depolymerization. Nature 2022;604:662–7.